THE JOURNAL OF PHYSICAL CHEMISTRY C
A JOURNAL OF THE AMERICAN CHEMICAL SOCIETY

pubs.acs.org/JPCC

Article

Scandia as the Oxygen Vacancy Stabilizer to Boost the Ionic Conductivity of Sc−Y-Codoped Zirconia

Shu-Hui Guan, Yi-Wen Wei, Cheng Shang,* and Zhi-Pan Liu*

Cite This: *J. Phys. Chem. C* 2026, 130, 2129−2138

Read Online

ACCESS | Metrics & More | Article Recommendations | Supporting Information

ABSTRACT: Scandia (Sc) and yttria (Y) codoped zirconia (ScYSZ) emerged as a promising candidate for high-performance solid electrolyte materials utilized in intermediate-temperature solid oxide fuel cells (IT-SOFCs). While it exhibits a record-high ionic conductivity (~0.10 S/cm at 800 °C), the physical origin of the superior performance remains poorly understood, limiting the further optimization and the application in IT-SOFC. Here, we construct the Sc−Y−Zr−O global neural network potential and explore systematically the thermodynamic landscape of ScYSZ across 65 different compositions (6.7−14.3 mol % dopants). From millions of candidate structures, we identify a thermodynamically stable cubic phase region at Sc/Y < 1 with $Y_2O_3 \geq 8$ mol %. Large-scale molecular dynamics simulations further show that ScYSZ at Sc_2O_3 = 3 mol % and Y_2O_3 = 8 mol % yields an exceptional ionic conductivity of 0.13 S/cm at 800 °C, surpassing conventional 8 mol % Y-stabilized zirconia (YSZ) by an order of magnitude. Our analysis reveals that the presence of Sc not only increases the O_v concentration by allowing ⟨111⟩ O_v−O_v pairs but also reduces the oxygen migration barriers markedly. Our results not only pinpoint the optimal ScYSZ composition for IT-SOFC applications theoretically but also establish a general framework for the rational design of advanced solid electrolyte materials.

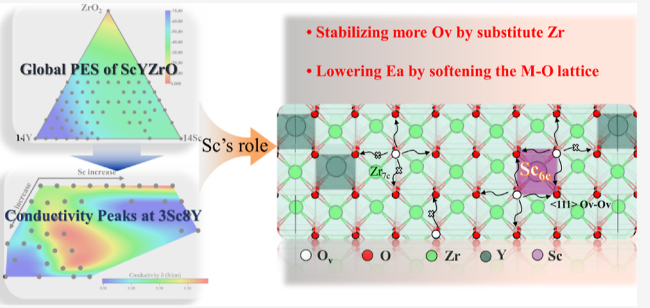

1. INTRODUCTION

The development of energy-efficient solid oxide fuel cells (SOFCs) hinges on the discovery of electrolyte materials with high ionic conductivity at intermediate temperatures (~800 °C).[1−5] Among all candidates searched,[6,7] ZrO_2-based electrolytes, particularly yttria-stabilized zirconia (YSZ) at 8 mol % Y_2O_3 (8Y), remain the leading choices due to their robust mechanical properties. The presence of the Y^{3+} dopant helps to create an O vacancy (O_v) and allow the O anion diffusion (conductivity). However, their operating temperatures are prohibitively high (>1000 °C) to achieve optimal conductivity (>0.1 S/cm).[8−10] In contrast, scandia-doped zirconia (ScSZ) can achieve the highest conductivity of all ZrO_2-based electrolytes but suffers from poor stability with a detrimental cubic-to-rhombohedral (β phase: no. 146, R3) crystal phase transition.[11,12] These limitations have spurred persistent interests in searching for optimal ternary metal oxides, particularly Sc−Y−Zr−O (ScYSZ), to simultaneously enhance conductivity and structural stability.[13−16]

Whether there is an optimal Sc/Y/Zr ratio, i.e., Sc_2O_3/Y_2O_3/ZrO_2, remains a fundamental question. The uncertainty originates from the conflicting reports from experimental data on ScYSZ conductivity synthesized from different methods.[13−18] For instance, Ciacchi et al. reported a monotonic increase in conductivity (from 0.17 to 0.29 S/cm conductivity at 1000 °C) with increasing Sc/Y ratio (1:7 to 7:1) at fixed total dopant levels (8−9 mol %).[19,20] Similar trends were observed in the 10 mol % dopant level.[15,21,22] Others found, however, conductivity peaks at specific compositions:[13,23] e.g., 0.0589 S/cm conductivity for 9Sc2Y (11 mol % dopants) at 800 °C,[13] or a maximum conductivity of 0.13 S/cm at 900 °C for 7Sc3Y, decreasing to 0.09 S/cm for 9Sc1Y.[17] Kondoh et al. identified 3Sc8Y as the optimal ratio (~0.17 S/cm at ~1000 °C) when partially substituting Sc into 8Y.

The discrepancies in these findings highlight the need for atomic-scale insights into the dopant/vacancy concentration, position, and atomic ordering, which experiments cannot resolve clearly.[24] However, this information is also difficult to obtain from traditional theoretical methods, which rely on empirical force-field-based simulations (e.g., Buckingham potentials[25]). The computed conductivity can deviate significantly from experiments (e.g., 0.20 S/cm vs 0.07 S/cm for 8.9Sc2.2Y at 885 °C),[21,26,27] which may be caused by their assumed atomic models without considering thermodynamically preferred cation/vacancy ordering[26] and utilizing rigid cation valences (e.g., Zr^{4+}) that neglect polarization

Received: December 3, 2025
Revised: January 18, 2026
Accepted: January 20, 2026
Published: January 28, 2026

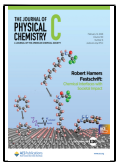

https://doi.org/10.1021/acs.jpcc.5c08205
J. Phys. Chem. C 2026, 130, 2129−2138

effects[21,27,28] and can lead to unphysical averaging of properties.

Here, we overcome these limitations by developing a quaternary Sc−Y−Zr−O global neural network (G-NN) potential, enabling systematic exploration of the energy landscape across 65 critical compositions (6.7−14.3 mol % dopants). Through large-scale molecular dynamics (MD), we identify the thermodynamically stable cubic phases and reveal a peak conductivity (0.13 S/cm at 800 °C) at 3Sc8Y, surpassing traditional 8Y by an order of magnitude. Mechanistically, we demonstrate, for the first time, that Sc, while being Sc^{3+}, being more like Zr^{4+}, facilitates O_v local accumulation along the ⟨111⟩ crystallographic direction in forming six-coordinated Sc and facilitates O diffusion by stabilizing the key Y−O_v pairs.

2. METHODOLOGY AND CALCULATION DETAILS

2.1. Global Neural Network Potential

All simulations based on G-NN potential were carried out by using LASP code, large-scale atomic simulation with neural network otential (www.lasphub.com)[29] developed by our group. LASP integrates the global potential energy surface (PES) data generation using SSW global optimization,[30,31] G-NN potential training and large-scale atomistic simulations using G-NN potential.[32]

The G-NN potential employs the many-body function-corrected neural network (MBNN) architecture[33] utilizing the power-type structure descriptor (PTSD)[34] as the input layer. The MBNN follows the atomic NN architecture proposed early by Behler and Parrinello,[35,36] but allows the atomic NN to output a vector for constructing different many-body functions. Further details on the G-NN method and the SSW-NN method can be found in Supporting Information Section S1.

The Sc−Y−Zr−O quaternary G-NN potential was trained by learning the global PES data generated by SSW global optimization. It has a five-layer (489−112−80−80−5) feed-forward NN structure, in total 265,348 fitting parameters, where five many-body functions include one single-body (atomic energy from NN output), two two-body (15 and 3 Å cutoff radius, respectively), and two three-body functions (all 3.5 Å cutoff radius). The short-range two-body term primarily prevents atom clashes during simulations. The training Sc−Y−Zr−O data set consists of 46,587 structures, encompassing pure Zr, ZrO_x, Y_2O_3, Sc_2O_3, and mixed oxides with Y/Zr ratios ranging from ∼1:9 to ∼4:3 and Sc/Y/Zr ratios ranging from ∼14:1:86 to ∼1:14:86, that were calculated by plane-wave density functional theory (DFT) calculations[37] (see Supporting Information Table S1). The root-mean-square (RMS) errors for the energy and the force of the Sc−Y−Zr−O G-NN are 3.711 and 0.118 eV/Å, respectively.

To validate the G-NN potential, we benchmarked its accuracy against DFT results for low-energy structures relevant to this work. The low-energy benchmarking structures correspond to physically realistic ScYSZ systems at the target dopant concentrations and were largely excluded from the training data set, thereby providing an unbiased validation of the G-NN potential. The energy RMS error for these structures is 2.44 meV/atom (Supporting Information Table S2), confirming that the G-NN PES provides a high-fidelity approximation to the DFT PES. This accuracy enables efficient global structure searches and pathway determinations.

2.2. DFT Calculations

All plane-wave DFT calculations were performed using the Vienna Ab-initio Simulation Package (VASP) code.[38] The calculation setup is as follows: DFT functional at the level of generalized gradient approximation (GGA-PBE);[39] the kinetic energy cutoff being 450 eV; the projector augmented wave (PAW) pseudopotential[40] to describe ionic core electrons; the fully automatic Monkhorst−Pack K-mesh with 25 times the reciprocal lattice vectors[41] for the first Brillouin zone *k*-point; convergence criteria for SCF energy and ionic relaxation force as 1×10^{-5} eV and 0.01 eV/Å, respectively.

2.3. Global Minimum Exploration

To identify the global minimum (GM) for different low-doping ZrO_2 systems, we started by performing the random substitution of Sc, Y, and Zr cations in a large supercell (>320-atom) of cubic ZrO_2, while maintaining the charge-neural condition using the formal charges of ions. The substitution is thus either Y/Sc or jointly, which generates more than 10,000 likely configurations. By optimizing all these configurations, we selected >100 lowest-energy structures for the subsequent SSW global optimization. For each low-energy structure, over 5000 minima were visited by SSW, and in total, more than 3600,000 structure candidates are obtained (more detail in Supporting Information Table S3), from which the GMs at each composition are finally determined. It should be noted that at elevated Sc concentrations, the thermodynamically most stable structures may deviate from the cubic fluorite phase and evolve toward competing or mixed phases, such as the β phase or the monoclinic phase, as widely reported experimentally. Therefore, SSW was employed to perform an unconstrained global exploration of the PES at each dopant concentration without enforcing the fluorite framework, which is essential for reliably identifying thermodynamically stable ScYSZ structures.

2.4. MD Simulations and Conductivity Calculations

To identify the equilibrated volume (lattice), the initial structure at a target temperature for a given Sc/Y concentration was always relaxed using variable cell MD, i.e., the isothermal−isobaric (NPT) ensemble for 1 ns. The ion motion was then simulated by using the Nose−Hoover thermostat[42,43] (*NVT*) canonical ensemble at the fixed cell. Thanks to the high speed of G-NN potential calculations (>4 orders of magnitude faster than DFT calculations[44]), we can carry out the long-time MD simulation for these large systems up to 5 ns with a time step of 1 fs. The first 0.5 ns of the *NVT* simulation was assigned to equilibrate the system, and the statistical average of the anion diffusion was calculated over the remaining time. For analysis, the local relaxation was utilized to obtain the intrinsic structure for the structure snapshots taken from MD trajectories until the maximal force on the atom was below 0.01 eV/Å. The structural analysis methods are detailed in the following.

2.4.1. Radial Distribution Function. The average radial distribution functions (RDF), $g(r)$, for Zr−O_v, Y−O_v, Sc−O_v, and O_v−O_v pairs can be computed using eq 1

$$g_{X-O_v}(r) = \frac{V}{N_{O/O_v}} \frac{\frac{1}{N_X}\sum_{i=1}^{N_X} n_{O_v,i}}{4\pi r^2 \Delta r} \quad (1)$$

where X represents the centering Zr, Y, Sc, or O_v; $n_{Ov,i}$ is the number of O_v situated in between the distance r to $r + \Delta r$ from the centering X atom. The $g(r)$ is normalized by dividing the

https://doi.org/10.1021/acs.jpcc.5c08205
J. Phys. Chem. C 2026, 130, 2129−2138

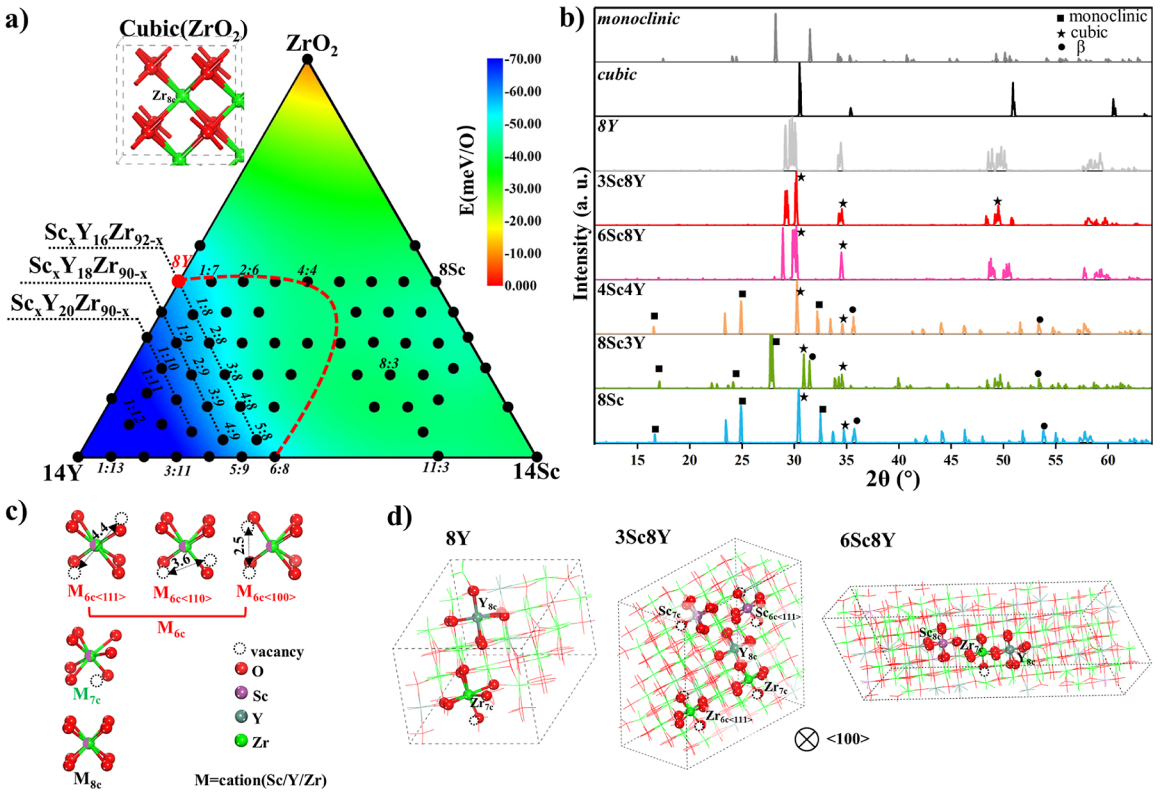

Figure 1. ScYSZ phase map from machine-learning global optimization. (a) Formation energy contour plot for the ternary phase diagram of the GM at varied $Sc_2O_3/Y_2O_3/ZrO_2$ ($Sc_2O_3 + Y_2O_3 + ZrO_2 = 100$) composition. (b) Simulated X-ray diffraction (XRD) patterns of GM structures from low-to-high Sc/Y ratio together with those of the standard monoclinic and cubic ZrO_2 phases. (c) Different types of cations categorized by the coordination number. The labeled distance between vacancies is in Å. (d) The atomic structures of three typical GMs (Sc/Y ratio = 0:8, 3:8 and 6:8) with key cation coordination types indicated, including 8-coordination Zr, Y, and Sc (Zr_{8c}, Y_{8c}, Sc_{8c}), 7-coordination Zr and Sc (Zr_{7c}, Sc_{7c}) and 6-coordination Zr and Sc (Zr_{6c} ⟨111⟩ and Sc_{6c} ⟨111⟩). Note that in GMs, there is neither Y_{7c} nor Y_{6c}.

total number of centering atoms in the cell, the number of anionic sites $N_{O/Ov}$ in the perfect cubic lattice ($= N_O + N_{Ov}$), and the volume of the cell (V).

2.4.2. O_v Location Analysis. In a perfect fluorite (cubic) structure, each O should be surrounded by four cations, i.e., at the center of a tetrahedron. We therefore identify O_v positions by identifying all tetrahedra formed by cations, each containing either one anion or one oxygen vacancy. To compute the RDF related to O_v, the vacancy coordinate can be determined by calculating the average value of the four nearby cations' coordinates.

2.4.3. Kinetics and Conductivity. The Einstein relation was used to determine the oxygen diffusion coefficients (D) from the slopes of mean square displacements of the oxygen atom (Δr^2) plotted versus simulation time (t)

$$D = \lim_{t\to\infty} \frac{<\Delta r(t)^2>}{6t} \tag{2}$$

The activation energies for oxygen diffusion (E_a) were computed by fitting the calculated diffusion coefficients to the standard Arrhenius equation

$$D = D_0 \exp\left(-\frac{E_a}{RT}\right) \tag{3}$$

The fitted E_a values were used to characterize the dependence of average diffusion barriers on different YSZ compositions. The conductivity of oxygen ions σ was finally derived from the Nernst−Einstein relation with the diffusion coefficient D

$$\sigma = \frac{q^2 DN}{VN_a}\left(\frac{F^2}{RT}\right) \tag{4}$$

where N_a is the Avogadro constant, q is the charge of the mobile ion (2 for oxygen), N is the number of oxygen atoms, and F is Faraday's constant.

3. RESULTS

3.1. Ternary Phase Diagram of ScYSZ and GM Structures

We started by exploring the phase space of bulk $Sc_{2a}Y_{2b}Zr_{1-2a-2b}O_{2-a-b}$ structures: over 3.6 million structures (see Methods 2.3) were searched, covering the composition Sc/Y ratios, i.e., a/b (Sc_2O_3 %/Y_2O_3 %), ranging from 14:0 to 0:14 at the total dopant concentrations from 6.7 to 14 mol %, in total 65 different compositions. Following the convention, we name $Sc_{2a}Y_{2b}Zr_{1-2a-2b}O_{2-a-b}$ as $\alpha Sc\beta Y$, where α/β indicates Sc/Y concentration in mol %, i.e., α = 2a, β = 2b. GM atomic structures of ScYSZ at these compositions are thus obtained, and the energetics of them are utilized to plot the ternary phase diagram for $Sc_{2a}Y_{2b}Zr_{1-2a-2b}O_{2-a-b}$ in Figure 1a. The color in Figure 1a reflects the relative formation energy (ΔE) of $Sc_{2a}Y_{2b}Zr_{1-2a-2b}O_{2-a-b}$ defined in eq 5 below, the energy per O anion relative to the cubic phase of bulk Y_2O_3, Sc_2O_3, and ZrO_2.

https://doi.org/10.1021/acs.jpcc.5c08205
J. Phys. Chem. C 2026, 130, 2129−2138

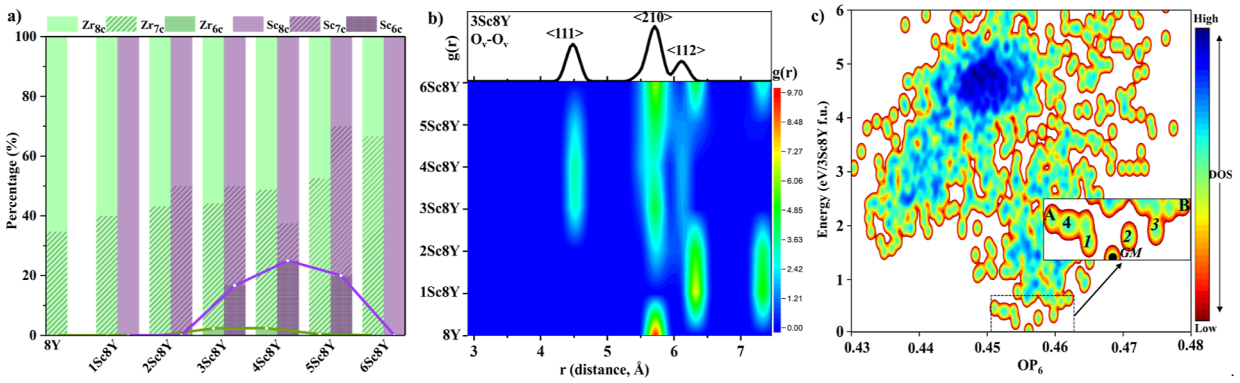

Figure 2. Analysis of 3Sc8Y structure features. (a) Average proportions of (Sc)Zr_{6c}, (Sc)Zr_{7c}, and (Sc)Zr_{8c} sites as a function of Sc_2O_3 concentration, based on the ten lowest-energy structures. The coordination of Y remains fixed at 8 and is not shown. The purple line indicates the variation in the Sc_{6c} site concentration, while the green line shows the trend in Zr_{6c} site concentration. (b) Radial distribution function, $g(r)$, of O_v−O_v pairs in different ScYSZ GMs at various Sc/Y ratios. The top panel corresponds to that of 3Sc8Y. (c) Global PES for 3Sc8Y using the OP_6 ~ E contour plot from the SSW-NN PES data and the inset shows an enlarged view of the region below 0.5 eV. OP_6: the structure order parameter with $l = 6$ (see OP_6 calculation details in Supporting Information).

$$\Delta E = \frac{E_{Sc_{2a}Y_{2b}Zr_{1-2a-2b}O_{2-a-b}} - (aE_{Sc_2O_3} + bE_{Y_2O_3} + (1-2a-2b)E_{ZrO_2})}{2-a-b} \quad (5)$$

Figure 1a shows that the low-energy structures of ScYSZ, materials tend to occur in the Y-rich region at the bottom left corner (deep blue zone). Specifically, from left to right, as the concentration of Sc by substituting Y increases, the color shifts from blue to green, indicating a rise in formation energy. For example, at a typical total dopant concentration of 8 mol %, starting from 1Sc7Y with ΔE −50.0 meV/O, the straight-right end composition 7Sc1Y has the higher ΔE of −36.7 meV/O, but as more Y substitutes Zr, the 1Sc13Y at the bottom has a much lower ΔE of −84.5 meV/O. On the other hand, with more Sc substituting Zr in the Y-rich region, as indicated by three parallel black dotted lines, no appreciable change in color occurs (all ΔE below −48.0 meV/O), reflecting that ΔE decreases only slightly after adding Sc. These results indicate that Y doping plays an important role in stabilizing cubic ZrO_2, and the energetically preferable doping mode of Sc is to replace Zr instead of Y. In other words, interestingly, Sc^{3+} cations function more like Zr^{4+} in forming ScYSZ ternary oxides.

By inspecting carefully the GM structures, we found that the crystal phases do vary upon the change of Sc/Y ratio. We outline roughly the phase transition region using the red dashed curve in Figure 1a, where the compositions on the left, corresponding to Y-rich systems with Sc/Y < 1, prefer the cubic phase as the GM, the same as YSZ at the same dopant concentration (see our previous work for YSZ phases[45]); the composition on the right, with the Sc/Y ratio greater than or equal to 1:1, representing Sc-rich systems, has the GM structures being close to that of ScSZ at an equivalent dopant concentration (Supporting Information Figure S2).

This trend of structure variation can be visualized in the simulated XRD patterns of ScYSZ compositions, as shown in Figures 1b and S3. At the low Sc/Y ratio, e. g., 3Sc8Y, the XRD pattern exhibits the typical cubic crystal features, with the major peak (2θ) at ~30.0°, corresponding to the crystal plane indices of (111) of the cubic ZrO_2. As the Sc_2O_3 concentration increases to Sc/Y = 1:1, e.g., 4Sc4Y, the XRD pattern resembles that of 8Sc and displays the multiple primary peaks at 24.9°, 30.3°, 35.5°, and 53.3°, which can be assigned to the (110) planes of the monoclinic phase, the (111) plane of the cubic phase, and the (110) plane and the (1̅ 10) plane of the rhombohedral (β) phase, respectively, indicating a mixed-phase formation. The further increase of Sc_2O_3 content, Sc/Y > 1:1, e. g., 8Sc3Y, leads to the features predominantly belonging to the monoclinic phase and β phase, namely, the major peak at 28.2° of the $(11\bar{1})$ plane and 30.9° of the (111) plane of the monoclinic phase, and the 31.5° of the (100) plane and the 53.3° of the (1̅ 10) plane for the β phase. Additionally, the XRD pattern also reflects the crystal lattice change at different Sc/Y ratios; in particular, the characteristic cubic (111) peak right-shifts with the increase of the Sc/Y ratio. For example, it is at 30.0° in 3Sc8Y and shifts to 30.3° in 4Sc4Y; at 29.5° in 1Sc7Y and shifts to 30.5° in 7Sc1Y (Supporting Information Figure S3). This is consistent with the fact that the ionic radius of Sc^{3+} (0.75 Å) is smaller than that of Y^{3+} (0.90 Å), leading to a contraction of the lattice parameters when Y is replaced by Sc.

Now, we focus on the atomic structures of the cubic phase in Y-rich systems with Sc/Y < 1:1 that have the lower formation energy. There are three distinct Zr coordination environments, as shown in Figure 1c, namely, the predominant 8-fold coordination (Zr_{8c}), the characteristic cation coordination in the bulk cubic phase; the 7-fold coordination (Zr_{7c}) with a single O_v nearby; and the less common 6-fold coordination (Zr_{6c}) with two O_v nearby. This coordination classification is also applicable to Sc and Y cations. Notably, the six-coordinated cations M_{6c} may adopt three possible geometrical configurations with reference to the perfect eight-coordination cubic ZrO_2, i.e., a linear 180° O_v-O_v arrangement with an O_v−O_v distance of ~4.4 Å that aligns along the ⟨111⟩ crystallographic direction, as reflected in the O_v−O_v RDF (Supporting Information Figure S4); a O_v-cation-O_v 109.5° angle arrangement with a O_v−O_v distance of 3.6 Å that aligns along the ⟨110⟩ plane; and a O_v-cation-O_v angle of 70.5° arrangement with the shortest O_v−O_v distance of 2.5 Å that aligns along the ⟨100⟩ plane. Among them, only the ⟨111⟩-aligned six-coordinated configuration is observed in the GM structures, indicating the repulsive nature of the O_v pair. This is supported by the absence of ⟨110⟩ and ⟨100⟩ features in the O_v−O_v RDF (Supporting Information Figure S4).

https://doi.org/10.1021/acs.jpcc.5c08205
J. Phys. Chem. C 2026, 130, 2129−2138

Table 1. Computed ScYZrO Material Properties at Selected Key Compositions[d]

Nomenclature	Formula	ΔE(meV/O)	Crystal phase[a]	δ^{cal} (1000 °C, S/cm)	δ^{exp} (1000 °C, S/cm)	References
8Y	$Y_4Zr_{23}O_{52}$	−54.3	c	0.17	0.16 ∼ 0.19	19,51
				0.01[b]	0.05[b]	
3Sc8Y	$Sc_6Y_{16}Zr_{86}O_{205}$	−53.0	c	0.29	0.10−0.21	13,23,52
				0.13[b]	0.06[b]	
4Sc9Y	$Sc_8Y_{18}Zr_{82}O_{203}$	−52.7	c	0.27	--	--
4Sc4Y	$Sc_8Y_8Zr_{92}O_{208}$	−40.7	c(P) + m/β(M)	0.23	0.22	14
6Sc3Y	$Sc_6Y_{12}Zr_{90}O_{207}$	−50.3	m/β(P)+ c(M)	0.001	0.24	20
		−32.7[c]	c	0.34	--	--
10Sc1Y	$Sc_{20}Y_2Zr_{88}O_{209}$	−52.5	m/β(P)+ c(M)	0.04	0.16	13,17,53,54
		−21.5[c]	c	0.35	0.05 ∼ 0.20[b]	

[a]Letters in parentheses indicate P: Predominant; M: Minority. The solid phases include cubic (c), monoclinic (m), and rhombohedral (β) phases. [b]The conductivity at 800 °C to compare with those at 1000 °C. [c]Selected high-energy phase for the purpose of comparison with the GM phase (the one above with the lower ΔE). [d]Listed data includes computed formation energy ΔE, crystal phase, and the conductivity from our MD simulations δ^{cal} and experiments δ^{exp} (see listed references).

Figure 1d illustrates the atomic structures of three representative compositions (8Y, 3Sc8Y, and 6Sc8Y) and highlights the distinct coordination of cations. In 8Y, Zr exists as Zr_{8c} and Zr_{7c}, while Y remains exclusively Y_{8c}, i.e., no O_v nearby Y. 3Sc8Y introduces ⟨111⟩-aligned Zr_{6c} and Sc_{6c} configurations. At higher O_v concentrations, such as 6Sc8Y, O_v forms exclusively near Zr, resulting only in Zr_{7c} and eliminating all six-coordinated species. This shift is reflected in the cation-O_v RDF, where O_v becomes increasingly associated with Zr (Supporting Information Figure S4).

With this interesting finding on the emergence of Zr_{6c} and Sc_{6c}, we selected ten lowest energy structures of αSc8Y (α = 0−6) and obtained the cation statistic for each coordination type, as shown in Figure 2a. The initial emergence of six-coordinated cations does occur at the 3Sc8Y composition, where the population of Zr_{6c} peaks at 2.33% (the green curve) and that of Sc_{6c} is 16.7% (the purple curve). The population of Sc_{6c} peaks at 4Sc8Y, reaching 25% of all Sc. Different from Sc and Zr, Y remains strictly eight-coordinate across all compositions (Figure 2a). This preferential O_v affiliation with Sc instead of Y could be attributed to two factors: (i) electrostatic effects. Our Bader atomic charge analysis reveals that Sc has an averaged lower Bader charge (+2.05 |e|) than both Y (+2.20 |e|) and Zr (+2.58 |e|), which suggests a lower energy cost in creating O_v formation nearby; (ii) Steric flexibility. Sc^{3+} has a smaller ionic radius (0.75 Å) compared to Y^{3+} (0.90 Å), which allows the greater bond-length variation and the release of O_v-induced local strain in accommodating O_v. Indeed, we note that the Sc−O bond length can vary largely in one single system; for instance, 12.8% in 3Sc8Y, being much larger than that of the Y−O bond length in the same structure, 6.3%.

Along with the cation coordination number variation, the O_v distribution in the solids also changes at different Sc/Y ratios. We plot the contour maps of the O_v−O_v RDF for the αSc8Y series in Figure 2b, which indicates the O_v intensity using a color from blue to red. The original RDF for 3Sc8Y is shown on the top of the figure. We note that a distinct feature of the compositions from 3Sc8Y to 5Sc8Y is a prominent ⟨111⟩-oriented peak at 4.4 Å, followed by secondary peaks at 5.8 Å ⟨210⟩ and 6.2 Å ⟨112⟩. This contrasts sharply with 8Y, where only a single peak at 5.8 Å ⟨210⟩ is observed. The new vacancy ordering at ⟨111⟩ stems from the preferential localization of O_v at first-nearest-neighbor (1NN) sites of Sc, as further corroborated by cation-O_v RDF analysis (Supporting Information Figure S4).

To understand how the stability of ScYSZ is influenced by the cation coordination and O_v distribution, we examined in detail the global PES of the material. As shown in Figure 2c, taking 3Sc8Y ($Sc_6Y_{16}Zr_{86}O_{205}$) as the example, we projected 5882 distinct structures collected from our global PES search within an energy window of <6 eV per formula unit onto an energy vs structure-fingerprint contour plot, with color (red → blue), indicating the local minima density. The high-density (blue) region corresponds to amorphous-like, high-energy states, which are 5 eV per formula unit (f.u.) above the GM. In the low-energy crystalline structure region, we identified five lowest-energy structures, labeled as GM and 1−4, which share the same cation position but different anion arrangements, suggesting that the cation position is critical to the oxide stability. Indeed, the higher-energy structures A and B (see the figure inset) start to change the cation distribution and are at least 0.45 eV per f.u. less stable than the GM.

As for the anion distribution, we note that if introducing a Y−O_v configuration (O_v nearby Y) in the GM of 3Sc8Y by altering a single O_v position, e.g., the structure 4 (Figure 2b), the energy rises by ∼0.39 eV; if modifying the O_v arrangement from the ⟨111⟩-aligned configuration in GM to a structure with enhanced ⟨210⟩ orientation intensity, as in structure 2, the energy increases by ∼0.24 eV; if there are only local distortions without changing the anion arrangement of GM, as in structure 1, there is only a ∼0.10 eV energy increase. These results indicate that the formation of the Y−O_v configuration is energetically most unfavorable in varying the anion location.

It is interesting to review the structure features observed in the experiments for the oxides. While there is no report on the structural features of Sc−Y codoped systems, several groups did report the O_v environment on single-doped ScSZ and YSZ. Using ^{45}Sc and ^{17}O NMR spectroscopy,[46] Huang et al. noticed that 8ScSZ has a significant accumulation of O_v around Sc. Using extended X-ray absorption fine structure (EXAFS), Kondoh et al. showed that the 8YSZ system has the presence of low-coordinated Zr atoms.[47] These studies support the direct adjacency of Zr or Sc to O_v, consistent with our theoretical findings from the GM search.

3.2. Conductivity Behaviors

With the GM structures and the thermodynamics phase diagram, we are now in a position to compute the conductivity for ScYSZ materials. To this end, a series of long-time MD

https://doi.org/10.1021/acs.jpcc.5c08205
J. Phys. Chem. C 2026, 130, 2129−2138

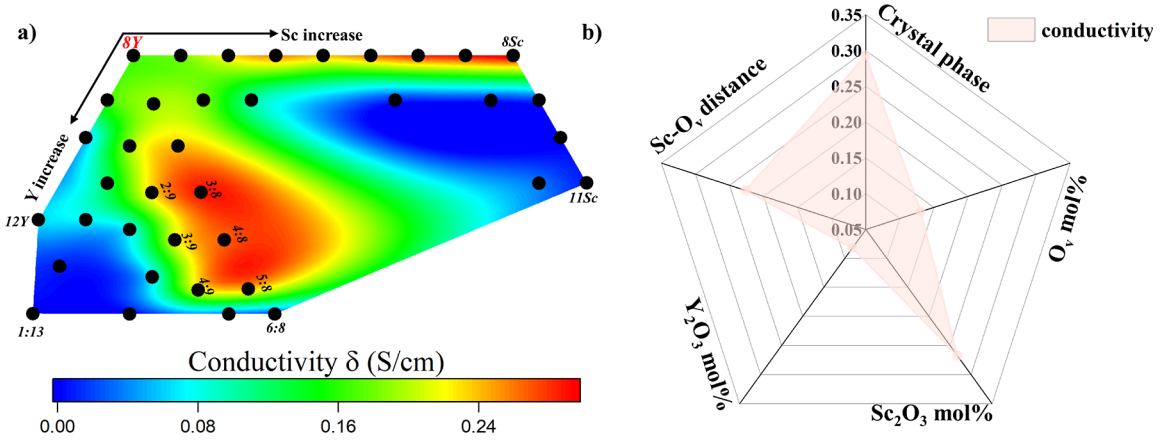

Figure 3. Conductivity behaviors obtained from MD simulations. (a) Conductivity contour plot at 1000 °C for 38 compositions; (b) radar chart of the influence of five factors on conductivity using the data in (a). The weights were determined using a random forest model.

simulations on 38 selected compositions were conducted, from which the O anion diffusion coefficients and the conductivity data are obtained following eq 4 (all conductivity values are provided in Supporting Information Table S4). These 38 compositions include mostly thermodynamically favored (low ΔE) cubic-phase compositions (Y-rich) and also several Sc-rich mixed-phase compositions that are utilized for comparison. Table 1 lists the key data of several typical compositions, including 3Sc8Y and mixed phases at high Sc compositions.

The conductivity data are plotted in Figure 3a as a contour map against the compositions, which shows, interestingly, a pronounced high-conductivity "hotspot" (red regions) centered around 8Y compositions. Notably, 3Sc8Y emerges as the optimal composition, achieving 0.29 S/cm at 1000 °C, nearly double the conductivity of 8Y (Table 1). At a lower temperature of 800 °C, 3Sc8Y still maintains a high conductivity of 0.13 S/cm, substantially surpassing that of 8Y (0.01 S/cm). Its neighbor composition 4Sc8Y also has a good conductivity, 0.27 S/cm at 1000 °C. The computed conductivity of 8Y and 3Sc8Y aligns well with the experimental data from Kondoh et al.[23] This result, on one hand, confirms the previous conclusion on the critical role of Y, where 8Y achieves the fastest O diffusion among single-doped zirconia (Supporting Information Figure S5), and, on the other hand, indicates that the promotional role of the second dopant, Sc cations, in enhancing ionic transport lies in, quite anti-intuitively, its substitution of Zr cation sites without interfering with the optimal concentration and the role of Y cations.

To disentangle the factors with competing influences on conductivity, we employed a random forest model to assess five critical variables: the crystalline phase type, the O_v concentration, the Sc_2O_3 concentration, the Y_2O_3 concentration, and the Sc−O_v distribution. The relative contributions obtained from the model can be visualized in the radar chart in Figure 3b. The chart highlights the impact weights of these factors, with each radial axis representing a specific variable and the length of the axis indicating its relative contribution to conductivity. It shows that the order of importance follows crystalline phase (29.3%) > Sc_2O_3 concentration (26.7%) > Sc−O_v distance (22.7%) > O_v mol % (13.1%) > Y_2O_3 mol % (8.2%). Not surprisingly, we see that the crystalline phase dominates the conductivity modulation, as the cubic phase provides the fastest channel for oxygen diffusion and the monoclinic phase is simply not a qualified oxygen conductor.[45,48] As for the importance of Sc, the concentration of Sc_2O_3 has a greater influence on the conductivity than the overall dopant concentration, underscoring the critical role of Sc-substitution for Zr in enhancing the conductivity. Conversely, Y_2O_3 primarily stabilizes the cubic phase rather than directly enhancing conductivity with its least importance in the sequence. It is worth noting that these multiple factors collectively reflect the key mechanisms previously proposed for YSZ systems, including the effects of O_v concentration and cation- O_v interactions,[48−50] which have been discussed in detail in our previous works.[45,48] Here, we bring these contributions together and quantitatively evaluate their relative importance within a single coherent framework, extending the analysis to the more complex ScYSZ system.

Our conductivity map establishes a theoretical framework to interpret the long-standing discrepancies in experimental conductivity data for high-Sc compositions. In particular, the experimental conductivity values for 10Sc1Y at 800 °C measured by different groups differs surprisingly by up to 4-fold[13,23,53,54] (Table 1), which, according to our radar chart in Figure 3b, should most likely be attributed to the synthetic procedure that produces samples with different/mixed crystal phases.[15,55,56] The computed conductivity data in Table 1 shows that the conductivity of the monoclinic/rhombohedral phase is ∼1−2 orders of magnitude lower than that of the cubic phase, even at the same composition (e.g., 0.04 for monoclinic-dominated 10Sc1Y vs 0.35 for cubic-dominated 10Sc1Y). Any local accumulation of Sc may be particularly detrimental in order to form the ideal cubic phase according to our results in Figure 1a. Structural analyses by several experimental groups indeed demonstrate that Sc-rich compositions predominantly crystallize into monoclinic/rhombohedral phases with embedded cubic/tetragonal inclusion.[57−59] Politava et al. reported that the increase of the β-phase content in 10Sc1Y by only ∼6% reduces the conductivity by 11.5% at 800 °C, i.e., from 0.052 to 0.046 S/cm.[13] This underscores the importance of the phase equilibrium among monoclinic, cubic, and β-phases, which largely dictates the conductivity.

3.3. Anion Diffusion Mechanism

To elucidate the origin of the Sc-enhanced conductivity at relatively low temperatures, we further analyzed anion diffusion kinetics for two representative materials, 8Y and 3Sc8Y. The diffusion rates were obtained over a temperature range of 800−1000 °C, and the corresponding apparent activation energies

https://doi.org/10.1021/acs.jpcc.5c08205
J. Phys. Chem. C 2026, 130, 2129−2138

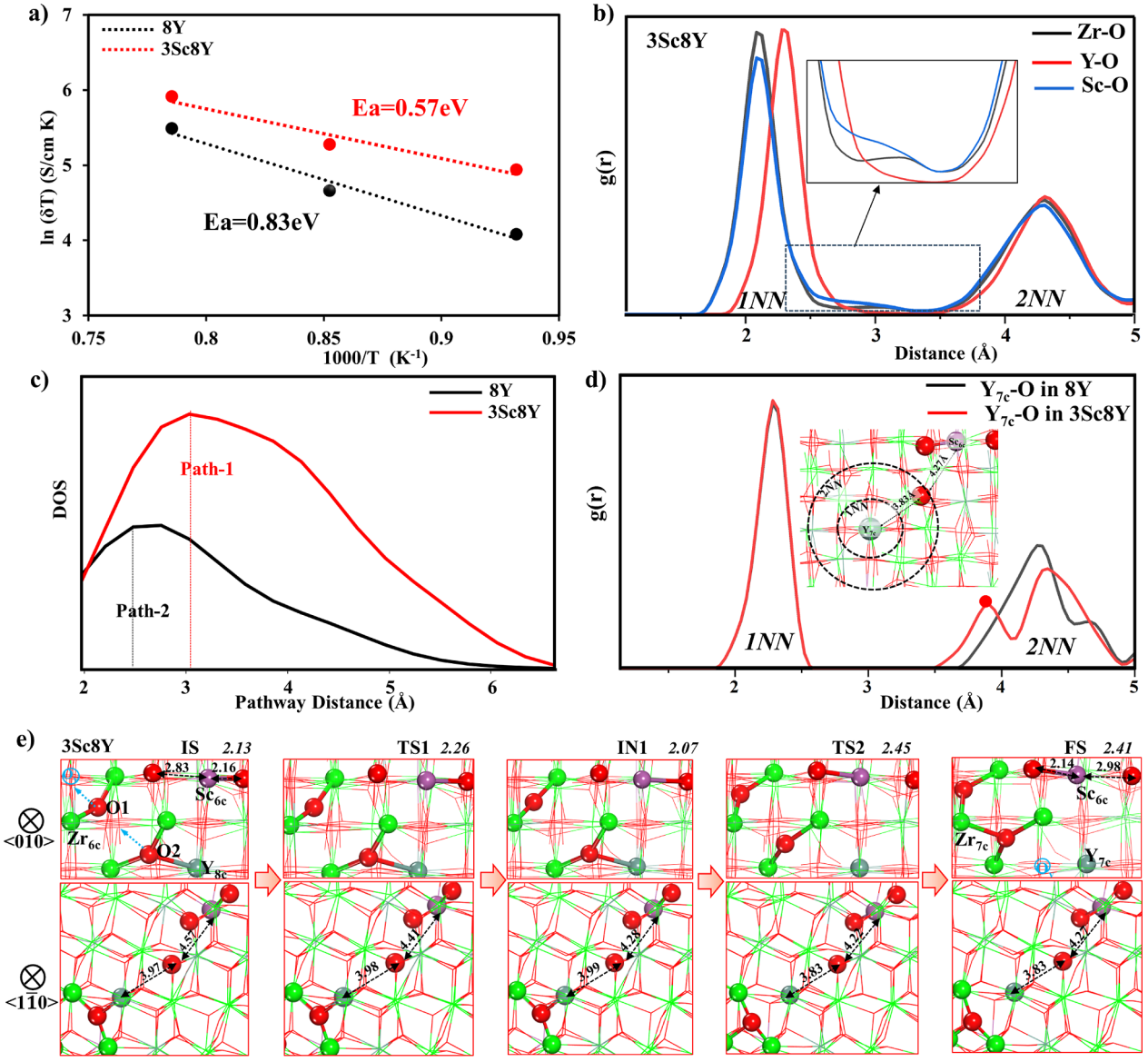

Figure 4. Oxygen anion migration mechanisms and pathways. (a) Arrhenius plot of the conductivity δ of 8YSZ and 3Sc8Y with respect to temperature from 800 to 1000 °C. (b) Average cation-oxygen RDF for 3Sc8Y at 1000 °C, highlighting the enhanced bond length flexibility of Sc−O compared to Zr−O/Y−O. (c) Reaction pathways obtained from MD trajectories at 1000 °C by plotting the density of the Euclidean distances of the pathways. (d) Y−O RDFs for 7-coordinated Y (Y_{7c}) sites in the FS structure of 8YSZ and 3Sc8Y, corresponding to the Path-1 mechanism. The inset shows the FS structure of Path-1 of 3Sc8Y, highlighting the shortened Y−O (2NN) distance at 3.83 Å. (e) Representative snapshots (100 fs intervals) of the dominant anion diffusion pathway type (Path-1) in 3Sc8Y, with relative energies (eV) indicated; two views along the ⟨010⟩ and the <11$\bar{0}$⟩ directions were shown to elucidate the structure evolution. Distances shown in the figure are given in Å.

were then extracted through Arrhenius fitting, as shown in Figure 4a. Not surprisingly, a substantial drop in the activation energy is found when Sc is added, i.e., from 0.83 eV in 8Y to 0.57 eV in 3Sc8Y. This kinetics data confirms that the presence of Sc does help to promote O diffusion and enhance the conductivity.

By comparing the MD trajectory with and without Sc, we found that 3Sc8Y has a more flexible cationic framework, where the Sc−O bond distance exhibits a large distribution. Figure 4b shows the averaged RDF of the cation-O pair in the MD trajectory at 1000 °C in 3Sc8Y. Compared to Zr−O and Y−O, Sc−O RDF has broader 1NN and 2NN peaks, reflecting a greater variability of the bond length. In addition, the averaged Sc−Sc RDF (Figure S6) shows a broad distribution in the first and second peaks, also reflecting the dynamic flexibility of the cationic framework. This characteristic facilitates a soft lattice rearrangement during oxygen migration. In contrast, the cation−O pairs in 8Y exhibit narrower peaks with sharply defined distance distributions, showing cations largely constrained to their ideal lattice sites (see Supporting Information Figure S7). It reflects the fact that both the Zr−O and Y−O bonds are rather rigid during O diffusion compared to Sc−O bonds.

We then examined in detail how the O diffusion is affected by the Sc dopant. By taking structures from MD trajectories at 1000 °C every 100 fs over a 40 ps simulation window, we relaxed them to their intrinsic states (local minima) and then connected them to generate 400 consecutive diffusion pathways, which form consecutive initial states (IS) and final states (FS). Finally, we searched the reaction pathways to

https://doi.org/10.1021/acs.jpcc.5c08205
J. Phys. Chem. C 2026, 130, 2129−2138

identify the reaction transition state (TS), if available, by using the doubled-ended surface walking (DESW)[60] method.

Among 400 pathway candidates, we captured 68 O diffusion events from 3Sc8Y, nearly three times more than that (24) from 8Y. The rest of the pathways have no O diffusion but only local structure distortive motion. These O diffusion pathways are summarized in Figure 4c by plotting the IS-FS distance, i.e., the O diffusion distance, versus the density of the states (DOS) of the pathway. It shows that most O diffusion pathways in 3Sc8Y have the IS-FS distance at ∼3.2 Å, labeled as Path-1 in the figure, suggesting a multi-ion cooperative migration within 100 fs, while in 8Y it primarily occurs at ∼2.5 Å pathways, labeled as Path-2 in the figure, reflecting a single O diffusion along the ⟨100⟩ direction (also see Figure S8a). Apart from the major peak position, the DOS of pathways in Figure 4c for all distances in 3Sc8Y are consistently larger than those in 8Y, indicating all O diffusion events occur much more frequently in 3Sc8Y.

By inspecting closely the O diffusion pathways, we observe that Sc dopant amplifies particularly the chance for migration of Y sites near Y sites appreciably: 20 events occurring near Y 1NN sites in 3Sc8Y, while only 4 events in 8Y. This is consistent with the fact that O_v has a higher chance to be at the 1NN neighborhood of Y in the MD trajectory at 1000 °C in 3Sc8Y, as reflected by the increased density of the first peak in the Y−O_v RDF (Figure S9). It suggests that while O_v dislikes Y as the first neighbor in the GM structure, the Y−O_v(1NN) pair plays an important role in the O diffusion kinetics. The presence of Sc helps to stabilize O_v−Y 1NN pairs and thus promote the diffusion.

We selected one representative O diffusion pathway to understand how Sc stabilizes the O_v−Y structure, as shown in Figure 4d,e. Path-1, a representative pathway occurring in 3Sc8Y, involves two O cooperative migrations, and the pathway involves both the coordination changes of nearby cations (e. g., $Zr_{6c}/Y_{7c}/Sc_{6c}$) and transient interstitial occupation of anions. This process comprises two elementary steps: first, the first O atom (O1) migrates along the ⟨100⟩ direction, bypassing a transition state (TS1) with a 0.13 eV barrier, forming intermediate IN1, where O1 occupies an interstitial site. Next, O1 migrates further with a nearby Y−1NN O2 migration along ⟨100⟩ cooperatively to achieve the second transition state (TS2, 0.32 eV barrier), ultimately yielding the final state (FS) featuring Y_{7c} coordination. We note that the analogous dual-O migration pathway in 8Y has a much higher barrier of 0.56 eV (Figure S8b).

Figure 4e shows clearly that the cooperative O diffusion in Path-1 of 3Sc8Y involves unusually significant Sc_{6c}−O bond length fluctuation, ∼2.1−2.9 Å, although the Sc is not directly linked with the O diffusion center. This further affects the geometry flexibility of the distal (second-shell) O that also contracts from 4.57 to 4.27 Å in the distance to Sc (Figure 4e). For the Y_{7c} in the reaction center, its distance with the 2NN O, Y−O(2NN) pairs, has a lowest value of 3.83 Å at the FS, as reflected by the Y_{7c}-O RDF in Figure 4d: a new peak (marked by a red circle) appears by splitting from the conventional ∼4.3 Å peak. Apparently, this compressed 2NN shell enhances the electrostatic interaction of the Y^{3+} center (a better charge screening), thereby stabilizing the otherwise unfavorable Y−O_v configuration. Overall, the flexibility of Sc−O bonds softens the local phonon modes, flattening the energy landscape of the oxygen cooperative migration by allowing a closer contact of Y_{7c} with O(2NN). The synergistic effect lowers the reorganization energy at TS2, explaining the reduced 0.32 eV barrier in 3Sc8Y compared with the 0.56 eV in 8YSZ.

To recap, our MD simulations and pathway analyses reveal the kinetic origin of the conductivity enhancement caused by Sc doping. The presence of Sc enhances oxygen mobility by stabilizing the key intermediates, the Y−O_v pairs, promoting cooperative multi-ion transport through a more flexible Sc−O framework, and thereby lowering the oxygen diffusion barrier and opening more long-range diffusion channels.

4. CONCLUSIONS

By developing the first global neural network (G-NN) potential for the Sc−Y−Zr−O quaternary system and conducting extensive stochastic surface walking (SSW) global optimization, this study systematically maps the PES of Y, Sc costabilized ZrO_2, spanning millions of structures across 65 compositions (6.7−14.3 mol % dopants). We identify a thermodynamically stable cubic phase region (Sc/Y < 1, Y_2O_3 ≥ 8 mol %), within which the Sc/Y = 3:8 composition achieves exceptional ionic conductivities of 0.13 S/cm at 800 °C. This enhancement arises from two synergistic effects. First, Sc^{3+} cations stabilize the close-contact O_v−O_v ⟨111⟩ pairs by forming Sc_{6c} cations, indicating Sc can effectively help Zr to accommodate O_v at a higher concentration, a key thermodynamic condition to achieve higher oxygen conductivity; second, Sc can reduce the O migration barrier kinetically by offering a flexible cation-O framework, which helps to stabilize the key Y_{7c}-O intermediate state. The critical roles of Sc can be understood as the consequence of its smaller ionic radius and smaller cationic charge compared to those of Y. Our findings establish the theory of Sc cation promotion on YSZ conductivity, offering general design guidance for IT-SOFC electrolytes and a framework for accelerating complex oxide discovery.

■ ASSOCIATED CONTENT

Supporting Information

The Supporting Information is available free of charge at https://pubs.acs.org/doi/10.1021/acs.jpcc.5c08205.

Global data set description; construction of Sc−Y−Zr−O ternary G-NN potential; benchmark of G-NN potential against DFT calculations; definition of the order parameter; thermodynamics convex hull and GM structures of ScSZ; XRD and RDF of other compositions; comparison between calculated conductivity and experimental conductivity; average RDFs of O_v−O_v and cation−cation at 1000 °C for xSc8Y; and RDFs and anion diffusion pathways for 8Y and 3Sc8Y (PDF)

■ AUTHOR INFORMATION

Corresponding Authors

Cheng Shang − *Collaborative Innovation Center of Chemistry for Energy Material, Shanghai Key Laboratory of Molecular Catalysis and Innovative Materials, Key Laboratory of Computational Physical Science, Department of Chemistry, Fudan University, Shanghai 200438, China;* orcid.org/0000-0001-7486-1514; Email: cshang@fudan.edu.cn

Zhi-Pan Liu − *Collaborative Innovation Center of Chemistry for Energy Material, Shanghai Key Laboratory of Molecular Catalysis and Innovative Materials, Key Laboratory of Computational Physical Science, Department of Chemistry,*

https://doi.org/10.1021/acs.jpcc.5c08205
J. Phys. Chem. C 2026, 130, 2129−2138

Fudan University, Shanghai 200438, China; orcid.org/0000-0002-2906-5217; Email: zpliu@fudan.edu.cn

Authors

Shu-Hui Guan − *The Education Ministry Key Laboratory of Resource Chemistry and Shanghai Key Laboratory of Rare Earth Functional Materials, Shanghai Normal University, Shanghai 200234, China; Collaborative Innovation Center of Chemistry for Energy Material, Shanghai Key Laboratory of Molecular Catalysis and Innovative Materials, Key Laboratory of Computational Physical Science, Department of Chemistry, Fudan University, Shanghai 200438, China;* orcid.org/0000-0001-9301-6084

Yi-Wen Wei − *Collaborative Innovation Center of Chemistry for Energy Material, Shanghai Key Laboratory of Molecular Catalysis and Innovative Materials, Key Laboratory of Computational Physical Science, Department of Chemistry, Fudan University, Shanghai 200438, China*

Complete contact information is available at: https://pubs.acs.org/10.1021/acs.jpcc.5c08205

Author Contributions

The manuscript was written through contributions of all authors. All authors have given approval to the final version of the manuscript.

Notes

The authors declare no competing financial interest.

■ ACKNOWLEDGMENTS

This work received financial support from the National Science Foundation of China (12188101, 92472113, and 22003040), the National Key Research and Development Program of China (2024YFA1509600), the Shanghai Science and Technology Commission Project (24ZR1455700), the Shanghai Municipal Education Commission ("AI-Driven Research Program"), the Fundamental Research Funds for the Central Universities (20720250005, 20720220011), the Science & Technology Commission of Shanghai Municipality (2024ZDSYS02), the robotic AI-Scientist platform of the Chinese Academy of Science, and the Tencent Foundation for the XPLORER PRIZE.

■ REFERENCES

(1) Gao, Z.; Mogni, L. V.; Miller, E. C.; Railsback, J. G.; Barnett, S. A. A perspective on low-temperature solid oxide fuel cells. *Energy Environ. Sci.* **2016**, *9* (5), 1602−1644.

(2) Fergus, J. W. Electrolytes for solid oxide fuel cells. *J. Power Sources* **2006**, *162* (1), 30−40.

(3) Wachsman, E. D.; Lee, K. T. Lowering the temperture of solid oxide fuel cells. *Science* **2011**, *334*, 935−939.

(4) Ni, M.; Shao, Z. Fuel cells that operate at 300° to 500°C. *Science* **2020**, *369* (6500), 138−139.

(5) Yu, H.; Jeong, I.; Jang, S.; Kim, D.; Im, H. N.; Lee, C. W.; Wachsman, E. D.; Lee, K. T. Lowering the Temperature of Solid Oxide Electrochemical Cells Using Triple-Doped Bismuth Oxides. *Adv. Mater.* **2024**, *36* (5), No. e2306205.

(6) Goodenough, J. B. Oxide-Ion Electrolytes. *Annu. Rev.Mater. Res.* **2003**, *33* (1), 91−128.

(7) Badwal, S. P. S. Zirconia-based solid electrolytes: microstructure, stability and ionic conductivity. *Solid State Ionics* **1992**, *52*, 23.

(8) Etsell, T. H.; Flengas, S. N. The electrical properties of solid oxide electrolytes. *Chem. Rev.* **1970**, *70* (3), 339−376.

(9) Steele, B. C. H.; Heinzel, A. Materials for fuel-cell Technologies. *Nature* **2001**, *414* (6861), 345−352.

(10) Kharton, V.; Marques, F.; Atkinson, A. Transport properties of solid oxide electrolyte ceramics: a brief review. *Solid State Ionics* **2004**, *174* (1−4), 135−149.

(11) Badwal, S. P. S.; Ciacchi, F. T. Oxygen-Ion Conducting Electrolyte Materials for Solid Oxide Fuel Cells. *Ionics* **2000**, *6*, 1−21.

(12) Yamamoto, O.; Arati, Y.; Takeda, Y.; Imanishi, N.; Mizutani, Y.; Kawai, M.; Nakamura, Y. Electrical conductivity of stabilized zirconia with ytterbia and scandia. *Solid State Ionics* **1995**, *79*, 137−142.

(13) Politova, T.; Irvine, J. T. S. Investigation of scandia−yttria−zirconia system as an electrolyte material for intermediate temperature fuel cells—influence of yttria content in system $(Y_2O_3)_x(Sc_2O_3)_{(11-x)}(ZrO_2)_{89}$. *Solid State Ionics* **2004**, *168* (1−2), 153−165.

(14) Raj, E. S.; Atkinson, A.; Kilner, J. A. Oxygen diffusion studies on $(Y_2O_3)_2(Sc_2O_3)_9(ZrO_2)_{89}$. *Solid State Ionics* **2009**, *180* (14−16), 952−955.

(15) Spirin, A.; Ivanov, V.; Nikonov, A.; Lipilin, A.; Paranin, S.; Khrustov, V.; Spirina, A. Scandia-stabilized zirconia doped with yttria: Synthesis, properties, and ageing behavior. *Solid State Ionics* **2012**, *225*, 448−452.

(16) Öksüzömer, F.; Vatansever, S.; Koç, S. N.; Deligöz, H.; Gürkaynak, M. A.; Somer, M. Preparation of Yttria-Stabilized Zirconia by the Reverse Microemulsion Method and the Effect of Sc and Ce Doping on Microstructure and Ionic Conductivity for Solid Oxide Fuel Cell Applications. *Int. J. Appl. Ceram. Technol.* **2011**, *8* (1), 42−48.

(17) Borik, M. A.; Bredikhin, S. I.; Bublik, V. T.; Kulebyakin, A. V.; Kuritsyna, I. E.; Lomonova, E. E.; Milovich, P. O.; Myzina, V. A.; Osiko, V. V.; Ryabochkina, P. A.; Tabachkova, N. Y. Structure and conductivity of yttria and scandia-doped zirconia crystals grown by skull melting. *J. Am. Ceram. Soc.* **2017**, *100* (12), 5536−5547.

(18) Kaneoko, H.; Jin, F.; Taimatsu, H.; Kusakabe, H. Electrical Conductivity of Zirconia Stabilized with Scandia and Yttria. *J. Am. Ceram. Soc.* **1993**, *76* (3), 793−795.

(19) Ciacchi, F. T.; Badwal, S. P. S. The System Y_2O_3-Sc_2O_3-ZrO_2: Phase Stability and Ionic Conductivity Studies. *J. Eur. Ceram. Soc.* **1991**, *7*, 197−206.

(20) Badwal, S. P. S.; Ciacchi, F. T.; Rajendran, S.; Drennan, J. An investigation of conductivity, microstructure and stability of electrolyte compositions in the system 9 mol% $(Sc_2O_3$-$Y_2O_3)$ $ZrO_2(Al_2O_3)$. *Solid State Ionics* **1998**, *109*, 167−186.

(21) Norberg, S. T.; Hull, S.; Ahmed, I.; Eriksson, S. G.; Marrocchelli, D.; Madden, P. A.; Li, P.; Irvine, J. T. S. Structural Disorder in Doped Zirconias, Part I: The $Zr_{0.8}Sc_{0.2-x}Y_xO1.9(0.0 \leq x \leq 0.2)$ System. *Chem. Mater.* **2011**, *23* (6), 1356−1364.

(22) Zhang, Y.-W.; Sun, X.; Xu, G.; Tian, S.-J.; Liao, C.-S.; Yan, C.-H. Co-doping effects of Y^{3+} and Sc^{3+} on the crystal structures, nanoparticle properties and electrical behavior of ZrO_2 solid solutions prepared by a mild urea-based hydrothermal method. *Phys. Chem. Chem. Phys.* **2003**, *5* (10), 2129.

(23) Kondoh, J.; Tomii, Y.; Kawachi, K. Changes in Aging Behavior and Defect Structure of Yttria-Fully Stabilized ZrO_2 with Sc_2O_3 Doping. *J. Am. Ceram. Soc.* **2003**, *86* (12), 2093−2102.

(24) Guan, S.-H.; Liu, Z.-P. Theoretical aspects on doped-zirconia for solid oxide fuel cells: From structure to conductivity. *Chin. J. Chem. Phys.* **2021**, *34* (2), 125−136.

(25) Schelling, P. K.; Phillpot, S. R.; Wolf, D. Mechanism of the Cubic-to-Tetragonal Phase Transition in Zirconia and Yttria-Stabilized Zirconia by Molecular-Dynamics Simulation. *J. Am. Ceram. Soc.* **2001**, *84* (7), 1609−1619.

(26) Kilic, M. E.; Soon, A. Understanding the Enhancement of Ionic Transport in Heterogeneously Doped Zirconia by Heterointerface Engineering. *J.Phys.Chem. C* **2018**, *122* (39), 22374−22388.

(27) Tung, K.-L.; Chang, K.-S.; Hsiung, C.-C.; Chiang, Y.-C.; Li, Y.-L. Molecular dynamics simulation of the complex dopant effect on the super-ionic conduction and microstructure of zirconia-based solid electrolytes. *Sep. Purif. Technol.* **2010**, *73* (1), 13−19.

(28) Miller, S. P.; Dunlap, B. I.; Fleischer, A. S. Effects of dopant clustering in cubic zirconia stabilized by yttria and scandia from molecular dynamics. *Solid State Ionics* **2013**, *253*, 130−136.
(29) Huang, S. D.; Shang, C.; Kang, P. L.; Zhang, X. J.; Liu, Z. P. LASP: Fast Global Potential Energy Surface Exploration. *Rev.: Comput. Mol. Sci.* **2019**, *9* (6), No. e1415.
(30) Shang, C.; Liu, Z.-P. Stochastic Surface Walking Method for Structure Prediction and Pathway Searching. *J. Chem. Theory Comput.* **2013**, *9* (3), 1838−1845.
(31) Shang, C.; Zhang, X.-J.; Liu, Z.-P. Stochastic surface walking method for crystal structure and phase transition pathway prediction. *Phys. Chem. Chem. Phys.* **2014**, *16* (33), 17845−17856.
(32) Huang, S.-D.; Shang, C.; Zhang, X.-J.; Liu, Z.-P. Material discovery by combining stochastic surface walking global optimization with a neural network. *Chem. Sci.* **2017**, *8* (9), 6327−6337.
(33) Kang, P. L.; Yang, Z. X.; Shang, C.; Liu, Z. P. Global Neural Network Potential with Explicit Many-Body Functions for Improved Descriptions of Complex Potential Energy Surface. *J. Chem. Theory Comput.* **2023**, *19* (21), 7972−7981.
(34) Huang, S. D.; Shang, C.; Kang, P. L.; Liu, Z. P. Atomic Structure of Boron Resolved Using Machine Learning and Global Sampling. *Chem. Sci.* **2018**, *9* (46), 8644−8655.
(35) Behler, J.; Parrinello, M. Generalized Neural-Network Representation of High-Dimensional Potential-Energy Surfaces. *Phys. Rev. Lett.* **2007**, *98* (14), 146401.
(36) Behler, J. Representing Potential Energy Surfaces by High-Dimensional Neural Network Potentials. *J. Phys.: Condens. Matter* **2014**, *26* (18), 183001.
(37) Kresse, G.; Furthmüller, J. Efficiency of ab-initio total energy calculations for metals and semiconductors using a plane-wave basis set. *Comput. Mater. Sci.* **1996**, *6* (1), 15−50.
(38) Kresse, G.; Furthmüller, J. Efficient iterative schemes for ab initio total-energy calculations using a plane-wave basis set. *Phys.Rev.B* **1996**, *54* (16), 11169−11186.
(39) Perdew, J. P.; Burke, K.; Ernzerhof, M. Generalized Gradient Approximation Made Simple. *Phys. Rev. Lett.* **1996**, *77* (18), 3865−3868.
(40) Kresse, G.; Joubert, D. From ultrasoft pseudopotentials to the projector augmented-wave method. *Phys. Rev. B:Condens. Matter* **1999**, *59* (3), 1758−1775.
(41) Monkhorst, H. J.; Pack, J. D. Special points for Brillouin-zone integrations. *Phys. Rev. B:* **1976**, *13* (12), 5188−5192.
(42) Hoover, W. G. Canonical dynamics: Equilibrium phase-space distributions. *Phys. Rev. A:At., Mol., Opt. Phys.* **1985**, *31* (3), 1695−1697.
(43) Nose, S. A unified formulation of the constant temperature molecular dynamics methods. *J. Chem. Phys.* **1984**, *81*, 511.
(44) Huang, S. D.; Shang, C.; Zhang, X. J.; Liu, Z. P. Material discovery by combining stochastic surface walking global optimization with a neural network. *Chem. Sci.* **2017**, *8* (9), 6327−6337.
(45) Guan, S. H.; Zhang, K. X.; Shang, C.; Liu, Z. P. Stability and anion diffusion kinetics of Yttria-stabilized zirconia resolved from machine learning global potential energy surface exploration. *J. Chem. Phys.* **2020**, *152* (9), 094703.
(46) Huang, H.; Hsieh, C. H.; Kim, N.; Stebbins, J.; Prinz, F. Structure, local environment, and ionic conduction in scandia stabilized zirconia. *Solid State Ionics* **2008**, *179* (27−32), 1442−1445.
(47) Kondoh, J.; Kikuchi, S.; Tomii, Y.; Ito, Y. Effect of Aging on Yttria Stabilizecl Zirconia Ill. A Study of the Effect of Local Sfructures on Conductivity. *J. Electrochem. Soc.* **1998**, *145* (5), 1550−1560.
(48) Guan, S.-H.; Shang, C.; Liu, Z.-P. Resolving the Temperature and Composition Dependence of Ion Conductivity for Yttria-Stabilized Zirconia from Machine Learning Simulation. *J. Phys. Chem. C* **2020**, *124* (28), 15085−15093.
(49) Shimojo, F.; Okabe, T.; Tachibana, F.O.; Kobayashi, M.; Okazaki, H. Molecular Dynamics Studies of Yttria Stabilized Zirconia.I. Structure and Oxygen Difusion. *J. Phys. Soc. Jpn.* **1992**, *61* (8), 2848−2857.
(50) Yamamura, Y.; Kawasaki, S.; Sakai, H. Molecular dynamics analysis of ionic conduction mechanism in yttria-stabilized zirconia. *Solid State Ionics* **1999**, *126*, 181−189.
(51) Kondoh, J.; Kawashima, T.; Kikuchi, S.; Tomii, Y.; Ito, Y. Effect of Aging on Yltria-Stabilized Zirconia I. A Study of Its Electrochemical Properties. *J. Electrochem. Soc.* **1998**, *145* (5), 1527−1536.
(52) Zhigachev, A. O.; Rodaev, V. V.; Zhigacheva, D. V.; Lyskov, N. V.; Shchukina, M. A. Doping of scandia-stabilized zirconia electrolytes for intermediate-temperature solid oxide fuel cell: A review. *Ceram. Int.* **2021**, *47* (23), 32490−32504.
(53) Agarkov, D. A.; Borik, M. A.; Bredikhin, S. I.; Burmistrov, I. N.; Eliseeva, G. M.; Kolotygin, V. A.; Kulebyakin, A. V.; Kuritsyna, I. E.; Lomonova, E. E.; Milovich, F. O.; Myzina, V. A.; Ryabochkina, P. A.; Tabachkova, N. Y.; Volkova, T. V. Structure and transport properties of zirconia crystals co-doped by scandia, ceria and yttria. *J. Materiomics* **2019**, *5* (2), 273−279.
(54) Irvine, J. T.; Dobson, J. W.; Politova, T.; García Martín, S.; Shenouda, A. Co-doping of scandia-zirconia electrolytes for SOFCs. *Faraday Discuss.* **2007**, *134*, 41−49.
(55) Joo, J. H.; Choi, G. M. Electrical conductivity of scandia-stabilized zirconia thin film. *Solid State Ionics* **2008**, *179* (21−26), 1209−1213.
(56) Agarkov, D. A.; Borik, M. A.; Bredikhin, S. I.; Burmistrov, I. N.; Eliseeva, G. M.; Kulebyakin, A. V.; Kuritsyna, I. E.; Lomonova, E. E.; Milovich, F. O.; Myzina, V. A.; Tabachkova, N. Y. Phase compositions, structures and properties of scandia-stabilized zirconia solid solution crystals co-doped with yttria or ytterbia and grown by directional melt crystallization. *Solid State Ionics* **2020**, *346*, 115218.
(57) Jeon, H.; Lee, I.; Oh, Y. Changes in high-temperature thermal properties of modified YSZ with various rare earth doping elements. *Ceram. Int.* **2022**, *48* (6), 8177−8185.
(58) Zhou, J.; Zheng, N.; Liu, C.; Wu, Y.; Omran, M.; Tang, J.; Zhang, F.; Chen, G. Crystal growth mechanism of nano nSc-Y/ZrO2 ceramic powders prepared by co-precipitation method. *Ceram. Int.* **2025**, *51* (9), 11878−11888.
(59) Xu, G.; Zhang, Y.-W.; Liao, C.-S.; Yan, C.-H. Doping and grain size effects in nanocrystalline ZrO2−Sc2O3system with complex phase transitions: XRD and Raman studies. *Phys. Chem. Chem. Phys.* **2004**, *6* (23), 5410−5418.
(60) Zhang, X. J.; Shang, C.; Liu, Z. P. Double-Ended Surface Walking Method for Pathway Building and Transition State Location of Complex Reactions. *J. Chem. Theory Comput.* **2013**, *9* (12), 5745−5753.

https://doi.org/10.1021/acs.jpcc.5c08205
J. Phys. Chem. C 2026, 130, 2129−2138